Analog Simulation of High-Harmonic Generation in Atoms

Javier Argüello-Luengo,[1,*] Javier Rivera-Dean,[1] Philipp Stammer,[1] Andrew S. Maxwell,[2] David M. Weld,[3] Marcelo F. Ciappina,[4,5,6] and Maciej Lewenstein[1,7]

[1] *ICFO—Institut de Ciencies Fotoniques, The Barcelona Institute of Science and Technology, Av. Carl Friedrich Gauss 3, Castelldefels, Barcelona 08860, Spain*

[2] *Department of Physics and Astronomy, Aarhus University, Aarhus C DK-8000, Denmark*

[3] *Department of Physics, University of California, Santa Barbara California, 93106, USA*

[4] *Department of Physics, Guangdong Technion—Israel Institute of Technology, 241 Daxue Road, Shantou, Guangdong 515063, China*

[5] *Technion—Israel Institute of Technology, Haifa 32000, Israel*

[6] *Guangdong Provincial Key Laboratory of Materials and Technologies for Energy Conversion, Guangdong Technion—Israel Institute of Technology, 241 Daxue Road, Shantou, Guangdong 515063, China*

[7] *ICREA, Pg. Lluis Companys 23, Barcelona ES-08010, Spain*

(Received 28 August 2023; revised 14 November 2023; accepted 18 January 2024; published 20 February 2024)

The demanding experimental access to the ultrafast dynamics of materials challenges our understanding of their electronic response to applied strong laser fields. For this purpose, trapped ultracold atoms with highly controllable potentials have become an enabling tool to describe phenomena in a scenario in which some effects are more easily accessible and 12 orders of magnitude slower. In this work, we introduce a mapping between the parameters of attoscience platforms and atomic cloud simulators and propose an experimental protocol to access the emission spectrum of high-harmonic generation, a regime that has so far been elusive to cold-atom simulation. As we illustrate, the benchmark offered by these simulators can provide new insights into the conversion efficiency of extended and short nuclear potentials, as well as the response to applied elliptical polarized fields or ultrashort few-cycle pulses.

DOI: 10.1103/PRXQuantum.5.010328

I. INTRODUCTION

Over the past three decades, progress in laser technologies has led to significant advances in our ability to manipulate and understand electron dynamics on their natural attosecond (10^{-18}-s) time scale [1–4]. This has triggered the development of a huge range of tools for probing and controlling matter, which includes high-harmonic spectroscopy [5], laser-induced electron diffraction [6,7], photoelectron holography [8,9], attosecond streaking [10,11], and reconstruction of attosecond harmonic beating by interference of two-photon transitions [12,13], to name only a small selection. One of the most prominent processes underlying some of these successes is high-harmonic generation (HHG), a highly nonlinear phenomenon where a system absorbs many photons of the driving laser and emits a single photon of much higher energy.

The experimental realization and interpretation of these complex processes have been guided most often by simplified theoretical descriptions that still capture the main properties of the dynamics. In the field of attoscience, simplifications such as only considering one or two active electrons, disregarding the interaction of the ionized electron with the parent ion during its propagation in the continuum, or performing saddle-point approximations have provided valuable quantitative predictions concerning HHG [14–16] and other phenomena [17–20]. Additional experimental regimes do, however, require a more complete description of the system, including those where multielectronic processes [16] or Coulomb nuclear potentials play a key role [21] (for reviews, see Refs. [9,22]). This has motivated an intense development of analytical and numerical methods aimed at pushing current computing capabilities.

To circumvent this computation complexity, analog simulation has become an enabling tool to access phenomena with highly controllable devices, the temporal and spatial scales of which are more favorable to measure than those

*javier.arguello@icfo.eu

naturally present in attosecond physics [23–25]. Experimental advances in the engineering of interactions now foster the simulation of quantum chemistry phenomena, such as molecular geometries [26,27], vibronic calculations [28,29], or the presence of conical intersections [30, 31]. Recently, this experimental benchmark of chemical processes has accessed the response of an atomic system to strong pulses in the regime where the energy imparted by the simulated laser field is strong enough to ionize the target atoms. This is the case of experiments where the incoming field is simulated by the curved shape of a waveguide [32], or by a shaken potential applied on a neutral atomic species [33], following early proposals where the correspondence to the static frame was introduced [34–36]. Going beyond the ionization regime, Sala *et al.* [36] have noted that controllable Zeeman or Stark shifts can also give access to the relevant regime of HHG in atomic simulators. However, the simulation of the HHG spectrum has so far remained elusive in these experiments where photons or neutral atoms mimic the oscillating electron, as no radiation is emitted by the associated neutrally charged simulated dipole. In this work, we show that current atomic platforms offer a unique opportunity to access and measure the emission spectrum of HHG through absorption measurements. Furthermore, the simulated Hamiltonian corresponds to the physical response of a *single-atom* target. This is in contrast with real experiments, where thousands of atoms are simultaneously driven to collect enough photons to resolve the spectrum, which challenges phase-matching conditions when a large ionization occurs under strong fields. The simulator thus provides an important bridge between experiments and theory, offering controllable experimental access to complex systems that otherwise can only be theoretically approximated.

The paper is structured as follows. First, we present key concepts on attoscience physics and ultracold-atom simulators that is of special interest for readers newly exposed to either of these areas. In particular, in Sec. II we discuss the status of current investigations in attosecond science and we motivate the different regimes that result from the frequency and strength of the laser field that drives the process. There, we introduce the HHG regime and some of its distinctive features. Next, in Sec. III we present current applications of analog quantum simulation, focusing our attention on the flexibility offered by atomic systems subjected to tunable light fields. There, we introduce an atomic simulator capable of mimicking the dynamics of an electron exposed to a strong oscillatory laser field and derive a mapping between the experimental parameters of the simulator and the relevant units encountered in attosecond science. We also devise a protocol to access the simulation of the emission yield in HHG, highlighting the range of parameters where this correspondence is valid. As an illustrative example, we show how one can use the simulator to study the effect that short pulses and the ellipticity of the incoming field have on the efficiency of HHG. In Sec. IV, we present further details on the experimental choice of atomic species and laser pulses that are needed to simulate specific targets of common studies in attosecond science and we discuss the main sources of errors that the experimental implementation would encounter, which we numerically benchmark. In Sec. V, we present an outlook of the avenue for exploration that the proposed simulator opens up.

II. HIGH-HARMONIC GENERATION

HHG stands as one of the most paradigmatic examples of strong-laser-field physics [1,3,14]. HHG is a highly nonlinear optical process in which a target gets subjected to a very intense ($I \sim 10^{13}$–10^{14} W/cm^2) and often short ($\tau \sim 5$–100 fs) laser pulse, which typically belongs to the infrared regime ($\lambda \sim 700$ nm–5 μm). As a result, the oscillating electron emits harmonics that could extend over frequencies hundreds of orders higher than the original driving field. The unique characteristics of HHG, including coherence, ultrashort duration, and high intensity, make it an exceptional source of extreme ultraviolet (XUV) radiation [37,38] and, nowadays, it configures the workhorse for the generation of attosecond pulses [39,40]. Consequently, HHG finds applications in various fields such as nonlinear XUV optics [41–48], attosecond science [1,14], molecular tomography [5] and high-resolution spectroscopy [49–52].

Although HHG is a process that has been observed in many different targets, such as atoms [14,53], molecules [54], solid-state systems [55,56], and nanostructures [4], in this work we will focus on simulating the HHG process in atoms. We shall now discuss the conditions required to generate high-order harmonics from atomic targets by introducing relevant parameters. The first is the so-called multiquantum parameter, $K_0 = I_p/(\hbar\omega)$ [22], where I_p is the ionization potential of the corresponding atom and ω is the frequency of the driving field. This parameter provides an estimate of the minimal number of photons required to ionize an electron from the atomic ground state. Here, we are particularly interested in the low-frequency limit, where $K_0 \gg 1$, indicating that ionization requires a significant number of photons. Furthermore, whether or not a multiphoton absorption process occurs also depends on the amplitude F_0, of the applied field. This motivates the introduction of the Keldysh parameter, $\gamma = \sqrt{I_p/(2U_p)}$ [14,22,57], where $U_p = e^2\xi_0^2/(4m\omega^2)$ is the ponderomotive energy, i.e., the average kinetic energy of an electron with mass m and charge e in the presence of an oscillating laser electric field of amplitude ξ_0 [see Fig. 1(a)].

In the case $K_0 \gg 1$, the multiphoton regime is observed when $\gamma \gg 1$, indicating that the field only slightly perturbs the atomic potential [see Fig. 2(a)]. The regime of interest for HHG processes corresponds to $\gamma \lesssim 1$, known as the

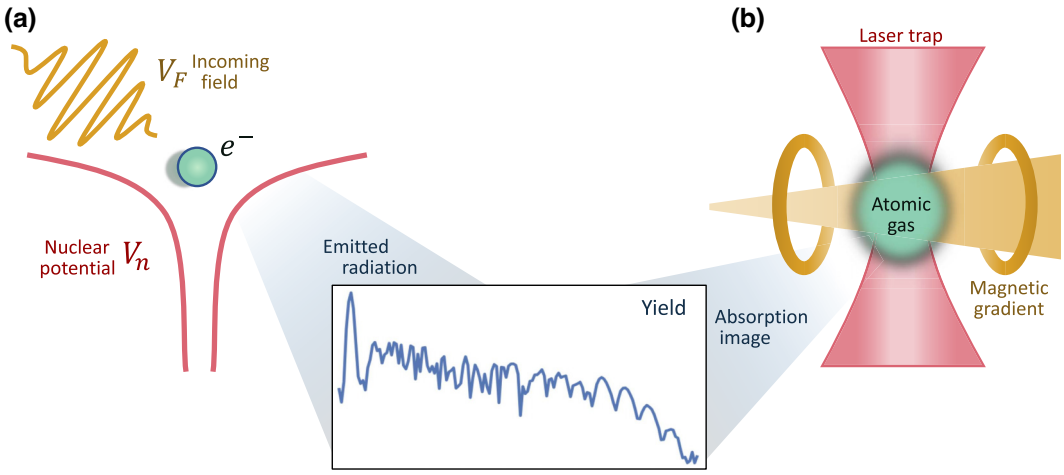

FIG. 1. (a) A schematic representation of HHG in atoms. (b) The proposed analog simulator. In (a), an ultrafast incoming field (brown) accelerates an electron (green) that was originally trapped by the nuclear Coulomb potential of the atom (red). The resulting oscillation of the charge emits radiation of characteristic harmonic frequencies (inset in blue). The same emission yield can be simulated on the simulator (b), where the characteristic frequencies are retrieved through absorption images of an atomic gas (green) that is trapped by a laser potential (red) and addressed by an external magnetic gradient that is tuned over time (brown).

tunneling regime, where the external field force is comparable to the atomic potential, which gets distorted and forms an effective potential barrier through which the electron can tunnel out [see Fig. 2(b)]. Finally, and for the sake of completeness, we have the regime of over-the-barrier ionization that, typically [58], happens when the electric field reaches a critical value that makes the barrier maximum coincide with the energy level of the electron ground state [see Fig. 2(c)].

Within the tunneling regime, the three-step model, also referred to as the *simple-man's model* [39,59,60], provides a powerful picture of the underlying electron dynamics behind HHG. The steps within this model are as follows: the electron (i) tunnels out from the parent atom through the barrier formed by the Coulomb potential combined with the dipole interaction of the field, (ii) oscillates in the continuum under the influence of the laser electric field and, if it passes around the vicinity of the nucleus, (iii) can recombine back to the ground state, emitting harmonic radiation. The energy of the emitted radiation upon recombination depends on the electronic kinetic energy at the moment of recombination and the ionization potential of the atom. However, the maximum kinetic energy that the electron can acquire from the field during its propagation is limited, leading to a natural cutoff frequency ω_c for the highest harmonic order in HHG, which is determined by $\hbar\omega_c = I_p + 3.17U_p$. The nonlinear character of the HHG process can be understood from its main features, namely, (i) a strong decrease in the amplitude of the low-order harmonics, (ii) a plateau where the harmonic yield is almost constant, and (iii) a sudden cutoff, given by the above-presented classical formula [39].

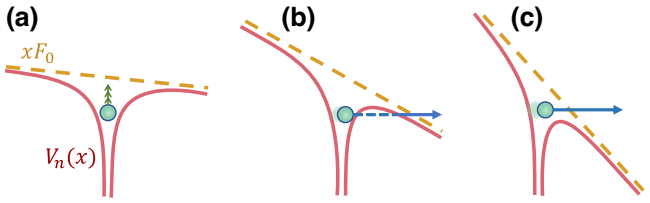

FIG. 2. A schematic representation of the different ionization mechanisms at the instant of maximum tilt for different values of the field strength. (a) $\gamma \gg 1$, such that it slightly perturbs the atomic potential, potentially leading to multiphoton ionization mechanisms. (b) $\gamma \lesssim 1$, such that the field is strong enough to allow for tunneling ionization. (c) The electric field has reached a critical value that makes the maximum of the barrier coincide with the energy level of the electron, leading to an over-the-barrier ionization mechanism. Note that in all these cases, we are working in the regime $K_0 \gg 1$.

Based on the previous discussion, it is evident that the polarization character of the driving field can have significant consequences on the generated harmonic radiation. For instance, when an elliptically polarized driver is considered, the ionized electron may miss the parent ion, resulting in the absence of the recombination event [59]. This phenomenon has been extensively studied in both experimental [61–66] and theoretical [67,68] works, demonstrating a reduced HHG conversion efficiency, i.e., the ratio between the outgoing and incoming photon fluxes, as the driving laser ellipticity increases. As an alternative strategy, a combination of two drivers that have different ellipticities and frequencies can be used to

generate bright phase-matched circularly polarized high harmonics, as shown in Refs. [69–73].

While we will focus on HHG, strong laser-matter interactions can also give rise to other fascinating phenomena, including above-threshold ionization (ATI) [3,74–77] and nonsequential double ionization (NSDI) [59,78–82]. In ATI, an electron is ionized by the strong laser field, surpassing the ionization threshold of the corresponding atom by absorbing more photons than are required for ionization. The typical observable measured in ATI is the photoelectron spectrum, which exhibits distinctive peaks at electron kinetic energies separated by the energy of a single photon of the driving field [74,76]. In the nonperturbative (tunneling) regime, these peaks form a plateau that extends over the electron energies on the order of $10U_p$ [76,83]. On the other hand, NSDI occurs when an ionized electron undergoes rescattering with its parent ion, resulting in the ionization of a second electron. This phenomenon is reflected in the ion yield, which exhibits a *knee* structure at a specific intensity threshold. The presence of this distinctive feature signifies a sudden change in the energy distribution of the emitted electron pairs, indicating a transition from sequential to nonsequential ionization processes [78,79].

Here, we demonstrate the capability of analog simulators to accurately replicate the key characteristics of the HHG processes in atoms. Specifically, they recover the main features of a typical HHG spectrum—a plateau extending for few harmonic orders followed by a cutoff—with an harmonic yield that reduces for increasing values of the ellipticity. We study how the conversion efficiency of the harmonics depends on the values of K_0 and γ and discuss how the simulated spectrum can be measured in practice for analog simulators, also providing estimates on relevant quantities toward feasible experimental implementations.

III. ANALOG QUANTUM SIMULATION

The numerical simulation of chemical problems generally requires us to describe many electrons that interact with external fields, the nuclei, and among themselves through Coulomb interactions. Even if one considers the nuclear positions to be fixed due to their larger mass (the Born-Oppenheimer approximation [84, 85]), this is an extremely challenging task, as the associated Hilbert space grows exponentially with the number of electrons.

Over the past few decades, an alternative route to studying electronic problems has emerged, based on using quantum devices that can better capture the complexity of the system. This idea was first proposed by Feynman as a way of preventing the exponential explosion of resources of quantum many-body problems [86] and later formalized by Lloyd [87]. Complementary to current efforts in digital simulation [88–90] (where the problem is first encoded as qubits and gates addressed by a general-purpose quantum device), simulators based on ultracold atoms have become an enabling tool, already addressing quantum matter phenomena that the most advanced classical computers cannot compute [91,92].

At low temperatures, the interaction among atoms can be highly engineered with external lasers, which allows us to induce a rich variety of effective Hamiltonians on a highly controllable platform [25,93]. Early experiments dealt with condensed-matter problems [94–96], detecting a transition between the superfluid and Mott-insulating phases of effective Hubbard models. More recently, atomic simulators have experimentally addressed problems related to high-energy physics, such as gauge theories, both in lattice geometries [97–99] and in the continuum [100]. An exciting perspective consists of extending the benefits of analog quantum simulation to the field of chemistry and the response of atoms and molecules to external fields. Soon after the first experimental realization of bosonic gases [101,102], the mapping between degenerate atomic gases and single-electron dynamics was noticed [34,103]. As compared to a real material, where many target atoms are present, here the simulated electron moves in a cleanly isolated environment. Furthermore, the typical energy scales of these experiments are in the range of kilohertz to megahertz, which provides a temporal magnification of the simulator, where attosecond pulses are associated with convenient time scales of microseconds to milliseconds, i.e., 10^9–10^{12} times slower. The additional tunability and accessibility of these simulators can thus offer a complementary tool with which to investigate ultrafast phenomena.

Using the Kramers-Henneberger correspondence, the shaking of the optical trap can mimic the effect of an external force [35,36,104], which has allowed for the recent experimental simulation of ATI processes using a bosonic gas of ^{84}Sr [33], where the kinetic energy of the simulated ionized electrons is accessed through a time-of-flight measurement (TOFM) of the atoms emitted during the shaking. However, extending this approach to the HHG regime is challenging, as the required inertial force corresponds to strong nuclear potentials (see Appendix A) and the associated photonic spectrum is neither emitted during the oscillation of neutral atoms nor directly revealed by the TOFM. The present contribution advances the study of HHG simulation in different directions. In particular: (i) we establish a correspondence between the experimental parameters in the simulator and the K_0 and γ parameters conventionally used in attosecond science, presenting specific configurations associated with standard choices of atomic targets and ionizing pulses; (ii) we show that the region of maximum HHG conversion efficiency can be accessed in atomic simulator platforms where the external pulses are simulated by existing Stark and Zeeman

shifts; and (iii) we introduce a scheme to experimentally access the generated harmonic spectra through absorption measurements of the atomic gas and characterize the main sources of error.

A. The simulator

Whenever multielectron processes can be neglected, the underlying physics of strong field processes can be described by a single-active electron. The dynamics of this electron are dictated by the Hamiltonian

$$\hat{H}(\mathbf{r},t) = \frac{\mathbf{p}^2}{2m} + V_n(\mathbf{r}) + V_F(\mathbf{r},t), \tag{1}$$

which accounts for its kinetic energy, the attractive nuclear potential, and the incident laser field, respectively. Following the dipole approximation, the interaction with a laser field linearly polarized along the $\mathbf{x}$ axis can be written as $V_F(\mathbf{r},t) = F(t)x$, where $F(t) = F_0 f(t)\sin(\omega t + \varphi)$ and $f(t) = \sin^2[\omega t/(2n_c)]$ is the carrier envelope for a pulse with n_c cycles and wave phase φ. Here, $F_0 = e\xi_0$ is the maximum force imparted by the field on the electron.

In this proposal, the dynamics of the electron inside the nuclear potential are simulated by an atomic Bose gas optically trapped by a laser beam, the spatial profile of which can be highly engineered, even dynamically, with the use of spatial light modulators [105,106] or digital-mirror devices [107,108]. Working in the single-active-electron approximation, this can allow us to engineer an effective potential for the valence electron based on an *ab initio* calculation of the multielectronic species, which can even provide quantitative agreement on the emitted spectrum, as theoretically studied in Refs. [109,110]. As a first experimental step for the simulator, here we will consider the natural Gaussian profile of a laser beam of waist r_0 and depth V_0 in a one-dimensional (1D) system

$$V_n(x,r_0) = -V_0 \exp\left[-x^2/(2r_0^2)\right]. \tag{2}$$

Similarly to the widely used atomic units, it becomes convenient to define the natural units of this system as $[\hbar] = [m] = [V_0 r_0] = 1$. In these units (which we denote as $[\cdot]$ throughout the text), the nuclear potential is fully characterized by the width of the trap, as it follows from the relation $[V_0] = [r_0]^{-1}$ and approximates a quantum harmonic oscillator whenever the associated zero-point motion of the oscillator is smaller than the waist of the beam, $[r_0] \gg 1$.

In Fig. 3(a), it can be seen that at short distances ($x/r_0 \ll 1$), the simulated Gaussian potential (dashed blue line) matches the widely used soft-core nuclear potential of the form $V_{sc}(x,r_0) = -1/\sqrt{x^2 + r_0^2}$ (red line; for further details, see Appendix B) [17,111]. To highlight this connection between the simulator and the soft-core potential,

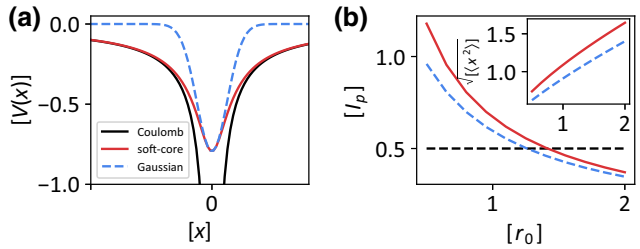

FIG. 3. (a) A comparison between the Coulomb potential, $-1/|x|$ (black line), the soft-core potential, $V_{sc}(x,r_0)$ (red), and the Gaussian potential $V_n(x,r_0)$ (blue) for $[r_0] = 1$. (b) The ionization energy associated with the Gaussian and soft-core potential (using the same color code as before), for different values of r_0. The black dashed line follows the hydrogenlike condition, $[I_p] = 0.5$. The inset indicates the average ground-state width. For details of the numerical calculation, see Appendix C.

in Fig. 3(b) we calculate the ionization energy associated with both nuclear potentials for different values of r_0, observing discrepancies smaller than 10% for $[r_0] > 1$. Focusing on the average width, $\sqrt{\langle x^2\rangle}$, of the ground state, the long-range polynomial scaling of the soft-core potential leads to more extended eigenstates than the short-range Gaussian trap [112,113] (see the inset), which can be experimentally explored by further shaping the laser beam. As compared to a real target with a fixed nuclear potential, the tunability offered by the simulator allows us to benchmark how the predictive power of conventional numerical methods is influenced by the range of the studied nuclear field. For example, this is relevant for the strong-field approximation, where the Coulomb potential throughout the excursion time of the electron is often numerically disregarded [14].

To mimic the effect of an incoming electric field under the dipole approximation, the atomic cloud is subjected to a time-dependent linear energy gradient, $V_F(\mathbf{r},t)$, which can be created by an optical Stark shift that is proportional to the intensity of an applied off-resonant laser field. In current platforms, a linearly varying intensity can be created with a spatial light-modulator [91], an acousto-optical device, or simply by using the slope of a Gaussian beam the intensity and position of which can be dynamically adjusted. For atomic levels that are sensitive to magnetic fields, one can alternatively rely on Zeeman shifts induced by linear magnetic field gradients created and modulated with current-carrying coils [114–116], as represented in Fig. 1(b).

B. Simulation of HHG emission yield

While there is no analog equivalent to the photons emitted during HHG, its emission yield can be accessed through the time-dependent dipole moment $d(t) = \langle\psi(t)|\,x\,|\psi(t)\rangle$ or its associated time-dependent

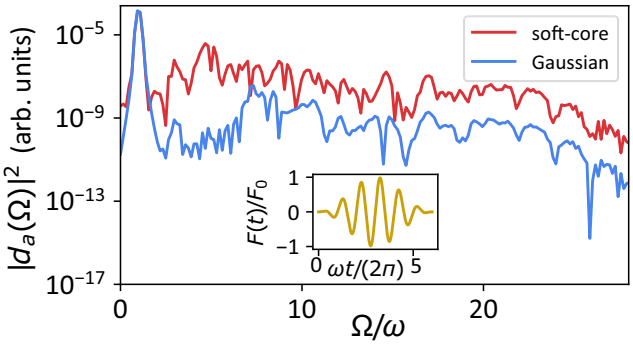

FIG. 4. The simulated emission yield, $d_a(\Omega)$, associated with a Gaussian (blue) and soft-core potential (red line). The inset shows a sinusoidal pulse, $F(t) = F_0 \sin^2(\omega t/2n_c)\sin(\omega t)$. The parameters are as follows: $[F_0] = 0.053$, $[\omega] = 0.057$, $[r_0] = 1.26$, and $n_c = 6$. For details of the numerical calculation, see Appendix C.

dipole acceleration, $d_a(t) = \langle\psi(t)|\,\ddot{x}\,|\psi(t)\rangle$, where $|\psi(t)\rangle$ denotes the atomic state at time t. In HHG experiments, the spectrum of energies for photons emitted over the duration of the laser pulse is characterized by the Fourier transform, $d_a(\Omega) = \int dt\, d_a(t) e^{-i\Omega t}$ [117].

In Fig. 4, we use a time-dependent Schrödinger equation (TDSE) to calculate the dipole acceleration $d_a(\Omega)$ in one spatial dimension. From Fig. 3(b), we choose parameters compatible with the hydrogen ionization potential $[r_0] = 1.26$, so that the corresponding dissociation energy is $[I_p] = 0.5$, and a six-cycle pulse with an associated laser field of wavelength 800 nm and intensity 10^{14} W/cm^2. There, we see that the short-range correspondence between the soft-core (red line) and Gaussian potentials (blue) translates into a qualitative agreement of the resulting harmonic spectrum.

To access this quantity in the simulator, one option consists of measuring the atomic spatial density and following the Ehrenfest theorem [118],

$$d_a(t) = -\langle\psi(t)|\,\nabla V_n(x)\,|\psi(t)\rangle\,, \tag{3}$$

where $\nabla V_n(x, r_0)$ denotes the gradient of the trapping potential. For the Gaussian trap expressed in Eq. (2), this gradient can be approximated as $\nabla_x V_n(x, r_0) \propto V_n(x + r_0/\sqrt{2}, r_0/\sqrt{2}) - V_n(x - r_0/\sqrt{2}, r_0/\sqrt{2})$. Therefore, an absorption measurement allows us to access $d_a(t)$ by quantifying the asymmetry in the atomic population for positions at a characteristic separation $r_0/\sqrt{2}$ from the center of the trap. By repeating the measurement at different times, we can recover the emission spectrum by Fourier transforming $d_a(t)$.

As an alternative, we can also access the time-dependent dipole velocity, $d_v(t) = \langle\psi(t)|\,\dot{x}\,|\psi(t)\rangle$, the spectra of which are related to the emission yield as $d_v(\Omega) = i d_a(\Omega)/\Omega$, in the case of finite pulses [119]. Interestingly, the velocity components of the atomic cloud at a given time can be conveniently accessed in the simulator through a TOFM, where the nuclear trap is suddenly released and the gas expands ballistically. Once the gas has expanded for a time τ beyond the initial size of the cloud, the velocity component, v, of the state of interest is associated with an absorption detection of the cloud at a distance $x = v\tau$ from the initial trap. Given that these separations are much larger that the size of the original cloud, this approach improves the accuracy of the reconstructed emission yield for a given spatial resolution.

In Fig. 5(a), we calculate the conversion efficiency [120]

$$\eta = \int_{\Omega-1}^{\Omega+1} |d_a(\omega)|^2 d\omega/|F_0|^2, \tag{4}$$

for one of the harmonics in the plateau region, a fixed nuclear potential $[I_p] = 0.5$, and different values of $[\omega] = [I_p]/K_0$ and $[F_0] = \sqrt{2[I_p]^3}/(K_0\gamma)$. In order to interpret the observed regimes, both K_0 and γ describe a complete set of parameters that characterizes the response of the simulated system to the oscillatory field. For example, expressed in natural units, the last harmonic $\Omega_c = \omega_c/\omega$ that becomes accessible below the cutoff energy is written as

$$\Omega_c = K_0\left(1 + 3.17/\gamma^2\right). \tag{5}$$

As expected, a higher yield appears above the continuous line, ⑤ where the condition $\Omega \leq \Omega_c$ is satisfied.

To enhance the conversion efficiency, it is also desirable not to be too deep in the tunneling regime. An optimal situation occurs when the maximum tilt of the nuclear potential, $F_0 r_0$, is comparable to I_p,

$$\gamma K_0 \approx [r_0]\sqrt{[I_p]}, \tag{6}$$

and we observe that the region of the largest conversion efficiency follows this heuristic scaling (red line ①).

Regarding the mapping to attoscience, the dipole approximation followed in Eq. (1) requires that the magnetic component of the incoming field can be disregarded. This imposes an upper bound ② on the intensity of the field, which is written as [121]

$$K_0/4 \ll \gamma^2[c]. \tag{7}$$

The prevention of relativistic velocities on the accelerated particle ($U_p \ll mc^2$) also induces a lower bound on the Keldysh parameter,

$$\sqrt{[I_p]} \ll \gamma[c], \tag{8}$$

which is less demanding than the dipole approximation throughout this region of greatest conversion efficiency

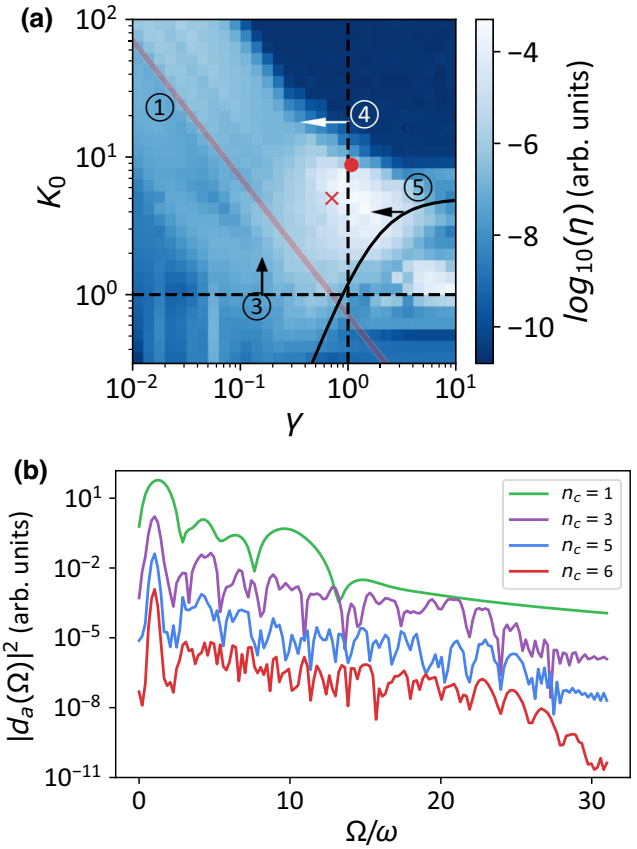

FIG. 5. (a) The conversion efficiency, η, of the fifth harmonic for the Gaussian potential in Fig. 4, a six-cycle pulse ($n_c = 6$), and different values of the Keldysh parameter (γ) and the multiquantum parameter (K_0). Red line ① follows the region where a higher efficiency is expected from Eq. (6), while dashed lines ③ and ④ describe the HHG region ($K_0 \geq 1$ and $\gamma \leq 1$, respectively). Line ⑤ follows the frontier where the selected harmonic is below the cutoff frequency in Eq. (5). The dipole approximation ②, associated with the upper bound in Eq. (7), lies above the represented range of values for K_0. The arrows point toward the region of validity for each of these conditions. The circled red marker indicates the Gaussian configuration in Fig. 4, while the crossed marker indicates the point $K_0 = 6.31$ and $\gamma = 0.81$, associated with $[F_0] = 0.171$ and $[\omega] = 0.108$. (b) The simulated emission spectrum of the latter configuration for incoming pulses, with a number of cycles running from $n_c = 6$ (red) to $n_c = 1$ (green). To improve visibility, an arbitrary vertical shift between the curves has been applied.

in Eq. (6) for $\gamma \ll 1$. In the natural units of the simulator, it can be seen that $[c] \sim 10^{11}$ for the parameters studied in Fig. 5(a), which places this upper bound above the represented range of values for K_0.

It should be noted that the harmonic radiation measured in an actual attoscience HHG experiment results from a collective phenomenon, involving 10^{10}–10^{12} atoms that emit coherent radiation *in phase*. When comparing theory and experiment, it is therefore mandatory to include macroscopic propagation effects, which is a formidable computational task that is only addressed by a limited number of models [122]. In this simulator, however, all atoms in the bosonic gas contribute to magnifying the effects manifested by a simulated single electron. The resulting harmonic spectrum is thus unaffected by the additional phase-matching condition that is often encountered in attosecond science experiments, providing clean access to the simulated single-atom dipole acceleration. Furthermore, the more favorable energy, spatial, and temporal scales in the simulator offer a benchmark that is less affected by the energy resolution, the uncertainty in the laser intensity and duration, or the limited dynamic range of spectroscopic measurements in ultrafast experiments [58].

The high tunability of the induced incoming pulse is also one of the advantages of the simulator, as compared with the fast high-intensity lasers that are typically needed in attoscience. For example, this allows us to easily simulate the response of the system to ultrashort pulses, a configuration that is otherwise demanding to access in real attosecond experiments. In Fig. 5(b), we show the simulated emission yield for pulses with different numbers of cycles. As the pulses get shorter, we observe that the plateau structure vanishes and the last harmonics disappear, even though the theoretical cutoff frequency ω_c only depends on the ionization energy and the ponderomotive energy, which are the same for all the curves. Intuitively, fewer interference processes can take place when the number of cycles of the pulse decreases, which reduces the number of harmonics that are visible on the emission spectrum as we approach $n_c = 1$ (green line). Focusing on this latter case, in Fig. 6 we simulate the response of the system to a single-cycle pulse ($n_c = 1$), for different values of K_0 and γ. When focusing on one of the lowest harmonics (the fifth one), we observe that the region of largest emission still remains well described by the different conditions introduced in Fig. 5(a).

In addition to the linearly polarized fields considered so far, the simulator also allows us to induce oscillations in a second axis, $F_{x(y)} = F_{0x(0y)} f(t) \sin[\omega t + \varphi + (\pi/2)]$, when we extend the systems to two dimensions. By controlling the ratio between the two amplitudes, i.e., the ellipticity $\varepsilon = F_{0y}/F_{0x}$, one can induce elliptic [$\varepsilon \in (0, 1)$] and circularly polarized fields ($\varepsilon = 1$). In HHG, the introduction of ellipticity in the laser beam leads to the deflection of the returning electron, causing it to deviate from its intended path toward the parent nucleus. This results in a decrease of the overlap between the wave packets of the returning electron and the initial bound state, as has been observed experimentally [61]. In Fig. 7, we calculate the change in the conversion efficiency of different harmonics as we change from a linear field ($\varepsilon = 0$) to an elliptically polarized field. As expected, we observe a decline in the intensity of harmonics as the ellipticity of the laser

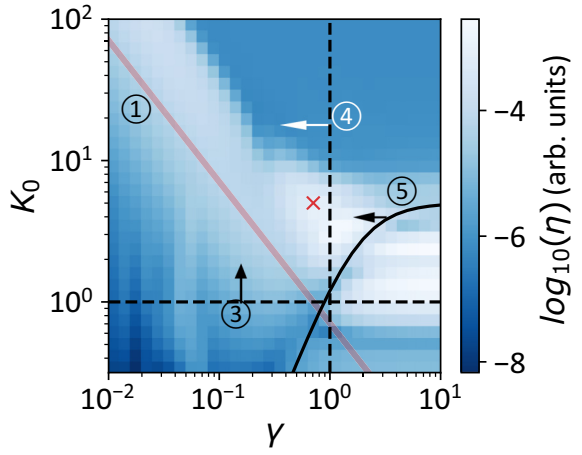

FIG. 6. The conversion efficiency, η, of the fifth harmonic for the Gaussian potential in Fig. 4, a single-cycle pulse, $n_c = 1$, and different values of the Keldysh parameter (γ) and the multiquantum parameter (K_0). Red line ① follows the region where a higher efficiency is expected from Eq. (6), while dashed lines ③ and ④ describe the HHG region ($K_0 \geq 1$ and $\gamma \leq 1$, respectively). Line ⑤ follows the frontier where the selected harmonic is below the cutoff frequency in Eq. (5). The arrows point toward the region of validity for each of these conditions. The crossed marker indicates the point $K_0 = 6.31$ and $\gamma = 0.81$, the emission spectrum of which is depicted in green in Fig. 5(b).

beam increases, which is more pronounced for the lowest harmonics.

IV. EXPERIMENTAL IMPLEMENTATION

At this point, it is worth exploring the feasibility of the experimental parameters associated with this implementation. For a fixed geometry $[r_0] = 1.26$ (associated with $[I_p] = 0.5$), the required nuclear potential scales as

$$V_0 = \frac{\hbar^2}{m r_0^2}[r_0]. \tag{9}$$

In the case of ^{84}Sr and a Gaussian beam with waist $r_0 = 1$ μm, the configuration $K_0 = 6.31$ and $\gamma = 0.81$ [illustrated in Fig. 5(b)] corresponds to parameters $F_0 = 1.55 \times 10^{-26}$ N, $\omega = 94.7$ Hz, and $V_0 = 7.22$ nK $\times k_B$. Using moderate conditions of 1 W of 532-nm light shaped to give a linear intensity gradient across an area of 100 μm × 100 μm, it is possible to achieve the required values of F_0 for ^{84}Sr atoms and even produce forces 2 orders of magnitude stronger. However, it can be observed that the associated trap depth, $V_0 \sim 10$ nK, is well below the trap depth of around 10 μK used in previous attoscience simulators with Sr [33].

The trap depth sets an upper limit to the temperature of the atomic clouds that can be trapped by the laser potential. To increase the range of allowed temperatures for the experiment, Eq. (9) indicates that more relaxed cooling conditions would benefit from choosing narrower beams and lighter atomic species. This is the case for ^{7}Li and $r_0 \sim 1$ μm, where the parameters needed to simulate the same attoscience configuration are $F_0 = 1.86 \times 10^{-25}$ N, $\omega = 1.14$ kHz, and $V_0 \sim 0.1$ μK $\times k_B$. The associated critical temperature is then consistent with state-of-the-art experiments [123]. As mentioned in Sec. III, for magnetic ground states, the oscillatory force can be applied by a tunable magnetic field gradient. In the case of the $|m_F| = 2$ hyperfine state of ^{7}Li, the easily attainable gradients of 50 G/cm translate into the required range of forces F_0 or even one order of magnitude larger.

In Fig. 8, we show the scaling of the trap depth with the beam waist for ^{84}Sr (green) and ^{7}Li (blue lines). We also show that more relaxed cooling conditions would appear in the simulation of weaker ionization energies, as we illustrate with dashed lines for the sodium first ionization energy, $[I_p] = 0.19$. Depending on the choice of atomic species and width of the trap, we observe a range of 3 orders of magnitude on the associated trap depth, which illustrates the flexibility that these simulators offer to access the regime of interest.

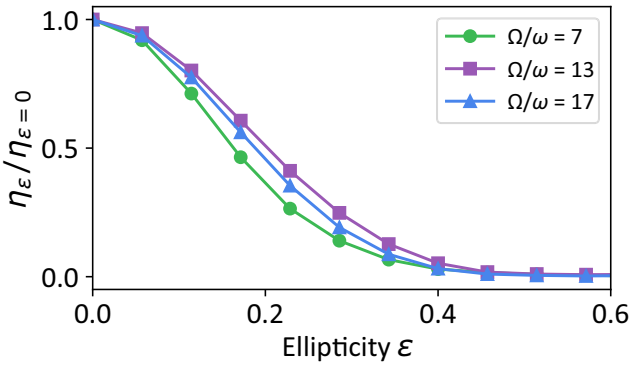

FIG. 7. The conversion efficiency of different harmonics (see legend) in a two-dimensional (2D) simulator along the x axis, as a function of the ellipticity of the incoming field. For each harmonic, the efficiency is normalized by the value at $\varepsilon = 0$. The parameters are as in Fig. 4 but now with a 2D Gaussian nuclear potential.

A. Further experimental considerations

The reconstruction of the dipole acceleration is also affected by experimental imperfections and limitations that need to be accounted for. Here, we numerically benchmark the main sources of error for the previous configuration, $K_0 = 6.31$, $\gamma = 0.81$, and $n_c = 6$, where a larger conversion efficiency is expected [crossed marker in Fig. 5(a)]. To quantify the effect of these imperfections, we calculate the relative error in the determination of the local maxima of the spectra for frequencies below the cutoff frequency,

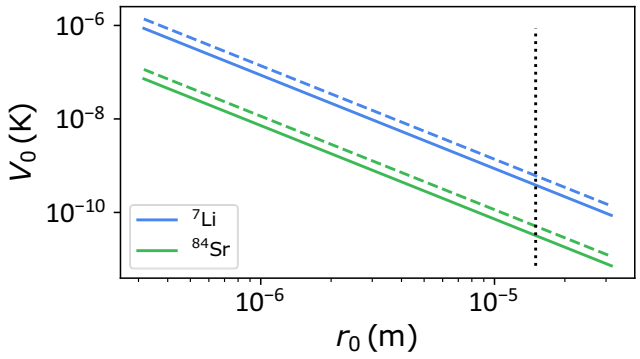

FIG. 8. The nuclear potential strength, V_0, as a function of the width of the beam, r_0, following Eq. (9). The green and blue continuous lines correspond to ^{84}Sr and ^{7}Li, respectively, for $[I_p] = 0.5$ (continuous line) and $[I_p] = 0.19$ (dashed line). The dotted line shows the condition $r_0 = 15$ μm of Ref. [33].

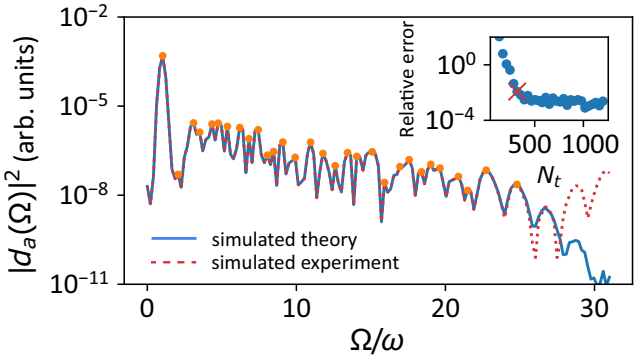

FIG. 9. Emission yield extracted from the discrete Fourier transform of $N_t = 300$ temporal intervals uniformly distributed along the duration of the pulse (red dotted line), as compared to the converged spectrum ($N_t = 3000$, blue line). Orange dots indicate the positions of local maxima before the cutoff energy. In the inset, we show the relative error of these local maxima for increasing number of temporal divisions, N_t, where the choice $N_t = 300$ is highlighted with a red cross, and the rest of parameters coincide with Fig. 5(b). See Appendix C for details on the numerical calculation.

which we highlight with orange dotted markers throughout Figs. 9–12.

In the experiment, the time-dependent dipole acceleration is measured at a finite set of times, $d_a(t_n)_{n=1\ldots N_t}$. The accuracy of the discrete Fourier transform,

$$d_a(\Omega) = \frac{1}{N_t}\sum_{n=1}^{N_t} d_a(t_n)e^{i\Omega t_n}, \tag{10}$$

then depends on the number of time points used in the reconstruction, which we consider to be uniformly distributed throughout the duration of the pulse. In the inset of Fig. 9, we calculate the relative error in the local maxima of the emission yield for different values of temporal divisions. We observe that a moderate number of time intervals, $N_t \sim 300$, provide an error of approximately 1%, which is enough to resolve the cutoff energy (see the red dashed line in Fig. 9).

Experimental errors in the time points used for the measurement, $\Delta t_n = |t_{\text{meas}} - t_n|$, would also manifest in the reconstructed yield. In the inset of Fig. 10, we calculate the relative error in the local maxima of the emission yield for different values of noise with standard deviation Δt around the time intervals t_n. We observe that moderate values $\omega\Delta t \sim 10^{-3}$ provide an overall relative error of approximately 10% in the local maxima, which is enough to resolve the cutoff energy (see the red dotted line in Fig. 10). Expressed in experimental units, this translates into a correct control of time in the order of approximately 10 μs. Overall, we see that the highest harmonics are the most sensitive ones to errors in the timing and number of time intervals, as they need to capture the rapidly oscillating response of the emission spectrum.

To quantify the time-dependent dipole acceleration from absorption measurements, one also needs to characterize the required accuracy in the determination of $d_a(t)$. In the inset of Fig. 11, we calculate the relative error in the local maxima of the emission yield for different values of relative error in the measurement of the time-dependent dipole acceleration, $\Delta d_a(t)/\overline{d_a}$, where $\overline{d_a} = \int_0^T |d_a(t)|/T$ is the temporal average throughout the pulse. We observe that $\Delta d_a(t)/\overline{d_a} \sim 1\%$ provides an accuracy in the emission yield that is enough to resolve the cutoff energy (see red dotted line in Fig. 11). We also observe that the highest harmonics, which have the smallest intensity,

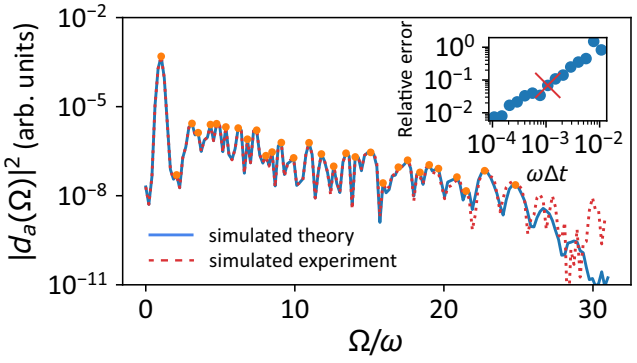

FIG. 10. Emission yield extracted from the discrete Fourier transform where the position of the temporal intervals randomly deviate from a uniform distribution with a standard deviation, $\omega\Delta t = 10^{-3}$ (red dotted line), as compared to the perfect spectrum (blue line). Orange dots indicate the positions of local maxima before the cutoff energy. In the inset, we show the relative error of these local maxima for increasing values of standard deviation, Δt, where the choice illustrated before is highlighted with a red cross. The rest of parameters coincide with Fig. 5(b).

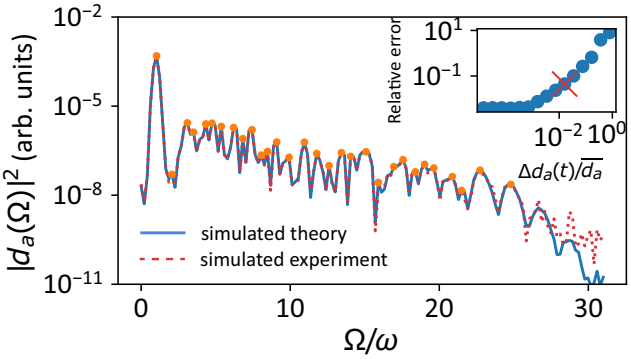

FIG. 11. Emission yield extracted from the discrete Fourier transform of the temporal dipole acceleration, whose values are randomly distorted with standard deviation, $\Delta d_a(t)/\overline{d_a} = 0.02$ (red dotted line), as compared to the perfect spectrum (blue line). Orange dots indicate the positions of local maxima before the cutoff energy. In the inset, we show the relative error of these local maxima for increasing values of standard deviation, $\Delta d_a(t)$, where the choice illustrated before is highlighted with a red cross. The rest of parameters coincide with Fig. 5(b).

are the most affected by a limited resolution. Following the TOFM approach to access $d_a(t)$, typical imaging lengths of 0.1–1.0 mm, associated with expansion times of $\tau \sim 10$–100 ms [124], can provide the required accuracy of 1% on the retrieved velocities for an atomic cloud that has an initial width of 1–10 μm before its ballistic expansion. Also, an error in the measured density of order $\Delta|\psi|^2 \sim 10^{-4}$ can be tolerated to reach the desired relative error of 1% in the extracted time-dependent dipole (see Appendix C). As the atomic cloud spreads over its different velocity components, this results in $N_{\rm ev} \sim 10^6$ single-atom events to reach the required accuracy on velocities and

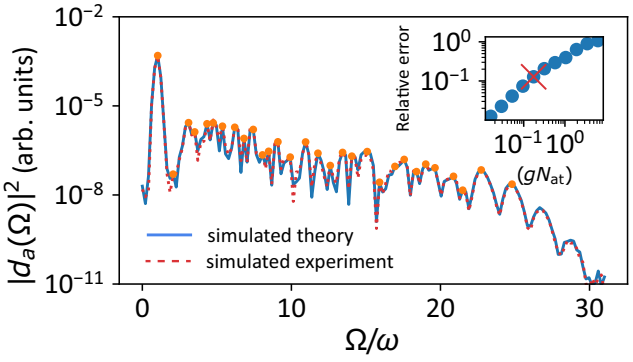

FIG. 12. Emission yield associated to an atomic cloud with interatomic interaction strength, $[gN_{\rm at}] = 0.2$ (red dotted line), as compared to the noninteracting case (blue line). Orange dots indicate the positions of local maxima before the cutoff energy. In the inset, we show the relative error of these local maxima for increasing values of interacting strength, where the choice illustrated before is highlighted with a red cross. The rest of parameters coincide with Fig. 5(b).

atomic densities during the TOFMs used to extract each instantaneous dipole acceleration.

Considering all these demands, one can estimate the overall experimental time needed to reconstruct the time-dependent dipole acceleration. For an atomic cloud with $N_{\rm at} \sim 10^4$ atoms [33] and an estimated running time of $\tau \sim 1$ s per experiment, the collection of enough statistics translates into a reasonable running time $\tau N_{\rm ev} N_t / N_{\rm at} \sim 10$ h. The major demand for resources comes from the repetition rate of the experiment and the required number of events needed to resolve the small variations in the absorption images. The first experimental realizations are then especially suitable for the simulation of the first harmonics in the plateau region, as they are associated with larger conversion efficiencies, reducing the number of independent measurements that are required and, with that, the overall experimental time.

As a final remark, we have seen that thousands of atoms in an atomic cloud are used to simulate the state of a single electron. Atoms do, however, experience interactions at distances characterized by the scattering length, a_s. In a mean-field approach, the effect of these interactions can be described by the Gross-Pitaevskii effective Hamiltonian, which depends on the atomic density at each point in space [125]:

$$\hat{H}_{\rm int}(\mathbf{r}, t) = \hat{H}(\mathbf{r}, t) + gN_{\rm at}|\psi(\mathbf{r}, t)|^2, \tag{11}$$

where $g = 4\pi\hbar^2 a_s/m$. In the inset of Fig. 12, we calculate the relative error in the retrieved spectrum for increasing values of interaction, observing an error below 10% for $[gN_{\rm at}] \sim 0.2$. As compared to the previously discussed sources of error, we observe in Fig. 12 that the presence of interactions distorts the entire spectrum and not just the largest harmonics. Expressed in experimental parameters, for a gas of $N_{\rm at} \sim 10^4$ atoms of ^{84}Sr, this interaction length corresponds to $a_s = r_0[gN_{\rm at}]/(4\pi N_{\rm at}[r_0]) \sim 10^{-12}$ m, which is 3 orders of magnitude shorter than the scattering length of the experiment in Ref. [33]. Using magnetic atoms such as Li, one could further rely on Feshbach resonances to engineer the required small values of the scattering length [126].

V. OUTLOOK

In this work, we have shown that the HHG emission yield can be simulated in current analog experiments using atomic clouds. We have characterized the response of the simulator to elliptic potentials and short pulses, as well as the main sources of errors for experimental implementations. Based on our calculations, we see that simulating attosecond dynamics by means of HHG is indeed possible with current analog simulators. They also offer a rich tunability on both the simulated incoming fields and the effective nuclear potential, where spatially modulated light

can engineer potentials [127,128] that mimic the long-range Coulomb attraction that ionized electrons experience during their excursion time. The flexibility of this approach offers several opportunities for the simulation of ultrafast processes:

(a) As nonclassical light sources become intense enough to drive the process of HHG [129], it reveals the limitations of semiclassical approximations [130]—such as the simple man's model, which treats the driving field purely classically. This implies new challenges for semiclassical methods to accurately predict the HHG spectrum [129] or the harmonic coherence properties [131] for such cases. Interestingly, even if photons do not have a counterpart in this simulator, the response of the system to nonclassical light (e.g., squeezed pulses) can be approximated by an effective photon-statistics force [132] that can potentially be included in the simulator due to the high tunability of the effective incoming field.

(b) Further extensions of this platform could focus on studying multielectronic processes. For example, through the use of shaken potentials in the ATI regime and the refined control provided by optical tweezers, each electron can be mapped to an individual fermionic atom in the trap. Extended atom-atom repulsive interactions provided by, e.g., magnetic dipoles [133], Rydberg dressing, [134,135] or mediating particles [136,137], allow us to directly tailor Coulomb corrections for a tunable degree of electronic repulsion. Going beyond the single-active-electron approximation for HHG, this offers the opportunity to simulate processes such as NSDI, where the electron-electron correlation plays a pivotal role and needs to be included in the theoretical models to satisfactorily describe the experimental observations [138–142].

(c) In this direction, the creation of tweezer arrays of controllable geometries can also assist with the understanding of rescattering processes that take place in the crystalline structure of materials [143, 144]. In this context, conventional theoretical analyses of HHG processes in solid-state media result in quasicontinuum harmonic spectra, lacking the clear presence of harmonic peaks that would be expected under ideal conditions. To make these harmonics distinctly visible, exceedingly small dephasing times (typically on the order of approximately 1 fs) are numerically employed [145], which may conflict with experimental observations [146,147] where the observed dephasing times are in the range of 15–50 fs. While recent theoretical studies have suggested that achieving numerical convergence is crucial to obtain well-resolved harmonic spectra without requiring extremely low dephasing times [148], others have tried to explain this phenomenon by considering the effect of propagation [149] or destructive interference between spatially long trajectories caused by the spatial distribution of laser fields [150]. In this regard, the use of a cleaner environment compared to real materials can offer a higher temporal and spatial resolution that can help discern the relevance of these interference effects. Furthermore, it can also be utilized to study the connection between the delocalized recombination of electrons [143,144,151] and the reduced dependence of the harmonic yield with the ellipticity of the driving field [55].

Overall, the tunability and accessibility of these experiments can be of significant value as a complementary tool to benchmark recently accessed experimental regimes and stimulate the development of novel numerical techniques and theoretical models, helping to reach a more profound understanding of the electronic response of atoms and materials to ultrafast and intense laser fields.

ACKNOWLEDGMENTS

We acknowledge Anna Dardia, Peter Dotti, Toshihiko Shimasaki, and Yifei Bai for helpful discussions on the experimental implementation. The ICFO group acknowledges support from: the European Research Council (ERC) Advanced Grant (AdG) "NOvel Quantum simulators—connectIng Areas" (NOQIA) (Grant agreement No. 833801); Plan National STAMEENA PID2022-139099NB-I00 project funded by MCIN/AEI/10.13039/501100011033 and by the "European Union NextGenerationEU/PRTR" (PRTR-C17.I1), FPI); the Ministerio de Ciencia y Innovation Agencia Estatal de Investigaciones (PGC2018-097027-B-I00/10.13039/501100011033, CEX 2019-000910-S/10.13039/501100011033, Plan National FIDEUA PID2019-106901GB-I00, FPI, QUANTERA MAQS PCI2019-111828-2, QUANTERA DYNAMITE PCI2022-132919 (QuantERA II Programme co-funded by European Union's Horizon 2020 program under Grant Agreement No 101017733), Ministry of Economic Affairs and Digital Transformation of the Spanish Government through the QUANTUM ENIA project call – Quantum Spain project, and by the European Union through the Recovery, Transformation, and Resilience Plan – NextGenerationEU within the framework of the Digital Spain 2026 Agenda; Proyectos de I+D+I "Retos Colaboraci" QUSPIN RTC2019-007196-7); MICIIN, with funding from the European Union (EU) NextGenerationEU (Grant No. PRTR-C17.I1) and by the Generalitat de Catalunya; the Fundació Cellex; the Fundació Mir-Puig; the Generalitat de Catalunya (European Social Fund FEDER and CERCA programs,

AGAUR Grant No. 2021 SGR 01452, QuantumCAT U16-011424, cofunded by the European Regional Development Fund (ERDF) Operational Program of Catalonia 2014–2020); the Barcelona Supercomputing Center MareNostrum (Grant No. FI-2023-1-0013); the EU (PASQuanS2.1, 101113690); the EU Horizon 2020 FET-Open "Optical Topologic Logic" (OPTOlogic) program (Grant No. 899794); and the EU Horizon Europe Program (Grant Agreement No. 101080086—NeQST), National Science Centre, and ICFO Internal "QuantumGaudi" project. European Union's Horizon 2020 program under the Marie Sklodowska-Curie grant agreement No 847648; "La Caixa" Junior Leaders fellowships, La Caixa" Foundation (ID 100010434): CF/BQ/PR23/11980043. J.R.-D. acknowledges funding from the Secretaria d'Universitats i Recerca del Departament d'Empresa i Coneixement de la Generalitat de Catalunya, the European Social Fund (L'FSE inverteix en el teu futur)–FEDER, and the ERC AdG Certification of quantum technologies (Grant agreement No. 834266). P.S. acknowledges funding from the EU Horizon 2020 research and innovation program, under the Marie Skłodowska-Curie Grant Agreement No. 847517. A.S.M. acknowledges funding support from the EU Horizon 2020 research and innovation program under the Marie Skłodowska-Curie Grant Agreement SSFI No. 887153. D.M.W. acknowledges support from the Air Force Office of Scientific Research (Grant No. FA9550-20-1-0240) and the University of California Santa Barbara NSF Quantum Foundry funded via the "Enabling Quantum Leap: Convergent Accelerated Discovery Foundries for Quantum Materials Science, Engineering and Information" (Q-AMASE-i) program under Grant No. DMR1906325. M.F.C. acknowledges financial support from the Guangdong Province Science and Technology Major Project ("Future Functional Materials under Extreme Conditions"—Grant No. 2021B0301030005) and the Guangdong Natural Science Foundation (General Program Project No. 2023A1515010871). Views and opinions expressed are, however, those of the author(s) only and do not necessarily reflect those of the European Union, European Commission, European Climate, Infrastructure and Environment Executive Agency (CINEA), or any other granting authority. Neither the European Union nor any granting authority can be held responsible for them.

APPENDIX A: THE KRAMERS-HENNEBERGER CORRESPONDENCE

One approach to simulating an oscillatory force on the simulating atom consists of shaking the trap potential. For simplicity, let us start by considering a 1D system trapped in the effective potential $V_n(x)$. When the potential is shaken with amplitude L and frequency ω, the effective atomic Hamiltonian is

$$\hat{H}_{\rm lab}(x,t) = \frac{p^2}{2m} + V_n[x + L\cos(\omega t)], \tag{A1}$$

with momentum p. To see the Kramers-Henneberger (KH) correspondence to an effective dipole force, one can follow the derivation in Ref. [152]. After the unitary displacement, $U_1 = \exp\left[-iL\cos(\omega t)p/\hbar + imL^2\omega\sin(2\omega t)/(8\hbar)\right]$, the rotated Hamiltonian, $H' = U_1 H_{\rm lab} U_1^\dagger + i\hbar(\partial_t U_1)U_1^\dagger$, can be written as

$$\hat{H}'(x,t) = \frac{[p - mL\sin(\omega t)]^2}{2m} + V_n(x) - \frac{mL^2\omega^2}{4}. \tag{A2}$$

Now performing a momentum displacement $U_2 = \exp[-imL\omega\sin(\omega t)x/\hbar]$, we find the KH frame

$$\hat{H}_{\rm KH}(x,t) = \frac{p^2}{2m} + V_n(x) + mL\omega^2\cos(\omega t)x - \frac{mL^2\omega^2}{4}, \tag{A3}$$

which, up to the energy shift $mL^2\omega^2/4$, corresponds to the static Hamiltonian with an additional effective oscillating force of strength $F_0 = mL\omega^2$. In this rotated frame, the initial state $|\psi_{0,\rm KH}\rangle = U_2 U_1 |\psi_0\rangle$, where $|\psi_0\rangle$ solves Eq. (A1), should correspond to the bound state of the trap, $|0\rangle$, which is also the state that can be easily prepared in the laboratory frame, $|\psi_0\rangle = |0\rangle$. The validity of this preparation is then dictated by

$$\alpha|_{t=0} \equiv |\langle\psi_{0,\rm KH}|\psi_0\rangle| = |\langle 0|U_2^\dagger U_1^\dagger|0\rangle| \sim e^{-1/\gamma^2}, \tag{A4}$$

which makes the shaking approach specially suitable for the multiphoton ionization regime, $\gamma \gg 1$, where $\alpha \sim 1$, but challenging in the HHG regime $\gamma \lesssim 1$.

Focusing on pulses with a finite number of cycles, the field is gradually introduced by the carrier envelope, which prevents the direct mismatch derived in Eq. (A4). Still, it should be observed that the atomic cloud cannot follow the shaken trap if the applied gradient of the potential, $\partial_x V_n(x)$, is weaker than the simulated inertial force of interest, F_0. For the Gaussian trap in Eq. (2), this semiclassical condition is written as $V_0 \gg F_0 r_0$, which challenges the experimental realization of the region $I_p \sim F_0 r_0$ introduced in Eq. (6), where the largest conversion efficiency of HHG is expected. This motivates the use of real oscillatory potentials to simulate this scenario, as introduced in the main text.

APPENDIX B: CONNECTION TO ATOMIC UNITS

Relevant chemical values are often expressed in atomic units (which we denote as $[\![\cdot]\!]$): $[\![\hbar]\!] = [\![m_e]\!] = [\![k_e]\!] = [\![e]\!] \equiv 1$. Conveniently, the Bohr radius (a_B) and the

Hartree energy, associated with the width and energy of the ground state of atomic hydrogen, can be written as

$$[\![a_B]\!] = \left[\!\left[\frac{\hbar^2}{e^2 m_e k_e}\right]\!\right] \equiv 1; \quad [\![\text{Hartree}]\!] = \left[\!\left[\frac{e^4 k_e^2 m_e}{\hbar^2}\right]\!\right] \equiv 1.$$

The Hamiltonian of our simulator is of a different form, as the nuclear potential $e^2 k_e / r$ is replaced by a Gaussian profile, $V_0 \exp\left[-x^2/(2r_0^2)\right] \approx V_0\left[1 - x^2/(2r_0^2)\right]$. The natural units of the system are now written as

$$[\hbar] = [m] = [e] = [V_0 r_0] \equiv 1.$$

Thus, the characteristic energy (E_0) and length scales (a_0) of the system are

$$[E_0] = \left[m\left(\frac{V_0 r_0}{\hbar}\right)^2\right] \equiv 1,$$
$$[a_0] = \left[\frac{\hbar^2}{m V_0 r_0}\right] \equiv 1.$$

In these units, the attoscience Hamiltonian in Eq. (1) can be written to the lowest order (up to a constant energy shift) as

$$\hat{H} \approx -\frac{\partial^2_{[x]}}{2} + \frac{[x]^2}{2[r_0]^3} + [F_0]\sin([\omega]t)\,[x],$$

which also matches the lowest-order expansion of the soft-core potential $V_{\rm sc}(x, r_0)$ for $[V_0 r_0] = 1$. Following this approach, the parameters of the simulator expressed in these units coincide with the same dimensionless value as the magnitudes of the real-life experiment expressed in atomic units. The connection with the other parameters of the model is finally derived as

$$[\omega] = \omega\hbar/E_0,$$
$$[F_0] = F_0 a_0/E_0,$$
$$[I_p] = I_p/E_0,$$
$$[c] = c\hbar/(a_0 E_0).$$

APPENDIX C: NUMERICAL METHODS

In the simulation of Fig. 4, we consider the atomic wave function extended over a length $x_{\rm max} = 180 r_0$, which is divided into 3000 discrete points. To prevent reflections at the edges, we apply a smooth attenuation mask of the form $\cos^{1/8}$ along a length $3r_0$ at the edges of the array [153].

To solve the time-dependent Schrödinger equation, we calculate the evolution of an initial ground state of the trapping potential, $|\psi(0)\rangle = |0\rangle$, under the time-dependent Hamiltonian in Eq. (A3). This evolution is Trotterized as [154]

$$|\psi(t)\rangle = e^{-\frac{i}{\hbar}\int_0^t H(s)ds}|0\rangle = \prod_{n=0}^{\lfloor t/\tau_0 \rfloor}\left(e^{-\frac{i\tau_0}{\hbar}H_x(n\tau)}e^{-\frac{i\tau_0}{\hbar}H_p}\right)|0\rangle + \mathcal{O}(\tau_0^2), \quad \text{(C1)}$$

where the operators $H_x(t) = V(x) + F_0\cos(\omega t)x$ and $H_p = p^2/(2m)$ are diagonal in real and momentum space, respectively. This simplifies their exponentiation by appropriately Fourier transforming the state from the real to the momentum space, where either of the Trotterized evolutions is diagonal. Throughout the figures, we have considered $\tau_0\omega = 0.01$.

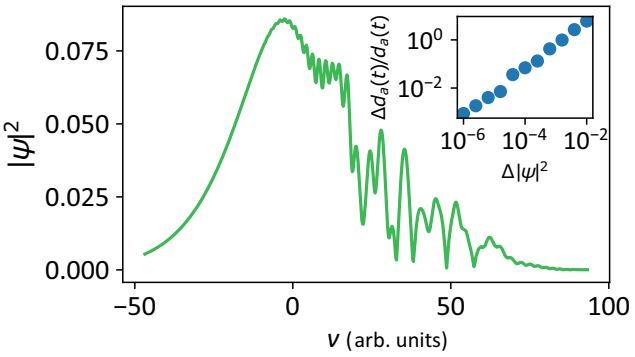

FIG. 13. The velocity components of the atomic cloud, $|\psi(v)|^2$, after half of an incoming six-cycle pulse is applied for the same parameters as in Fig. 5(b). The inset shows the relative error on the reconstructed dipole acceleration, $d_a(t = T/2)$, as we introduce Gaussian noise of standard deviation $\Delta|\psi|^2$ on the velocity components of the main figure. The markers indicate the average over ten random realizations.

In Fig. 13, we show the velocity components of the atomic cloud (corresponding to the squared wave function in momentum space) at a given instant of the driving. This curve can be measured in the experiment through TOFM, where momentum is mapped to different positions of the atomic cloud after a ballistic expansion of the gas. In the inset, we show that the relative error of the extracted dipole acceleration scales polynomially with the noise in the atomic density detection, providing an error smaller than 1% for $\Delta|\psi|^2 \sim 10^{-4}$. This indicates a desired accuracy for the experimental fluorescence measurements.

[1] F. Krausz and M. Ivanov, Attosecond physics, Rev. Mod. Phys. **81**, 163 (2009).

[2] P. Salières, A. L'Huillier, P. Antoine, and M. Lewenstein, in *Advances In Atomic, Molecular, and Optical Physics*, Vol. 41, edited by Benjamin Bederson and Herbert Walther (Academic Press, San Diego, 1999), p. 83.

[3] M. Lewenstein and A. L'Huillier, in *Strong Field Laser Physics*, edited by Thomas Brabec, Springer Series in Optical Sciences (Springer, New York, NY, 2009), p. 147.

[4] M. F. Ciappina, *et al.*, Attosecond physics at the nanoscale, Rep. Progr. Phys. **80**, 054401 (2017).

[5] J. Itatani, J. Levesque, D. Zeidler, H. Niikura, H. Pépin, J. C. Kieffer, P. B. Corkum, and D. M. Villeneuve, Tomographic imaging of molecular orbitals, Nature **432**, 867 (2004).

[6] T. Zuo, A. D. Bandrauk, and P. B. Corkum, Laser-induced electron diffraction: A new tool for probing ultrafast molecular dynamics, Chem. Phys. Lett. **4**, 313 (1996).

[7] H. Niikura, F. Légaré, R. Hasbani, A. D. Bandrauk, M. Yu. Ivanov, D. M. Villeneuve, and P. B. Corkum, Sub-laser-cycle electron pulses for probing molecular dynamics, Nature **417**, 917 (2002).

[8] Y. Huismans, *et al.*, Time-Resolved Holography with Photoelectrons, Science **331**, 61 (2011).

[9] C. F. de Morisson Faria and A. S. Maxwell, It is all about phases: Ultrafast holographic photoelectron imaging, Rep. Prog. Phys. **83**, 034401 (2020).

[10] M. Hentschel, R. Kienberger, Ch. Spielmann, G. A. Reider, N. Milosevic, T. Brabec, P. Corkum, U. Heinzmann, M. Drescher, and F. Krausz, Attosecond metrology, Nature **414**, 509 (2001).

[11] J. Itatani, F. Quéré, G. L. Yudin, M. Yu. Ivanov, F. Krausz, and P. B. Corkum, Attosecond streak camera, Phys. Rev. Lett. **88**, 173903 (2002).

[12] P. M. Paul, E. S. Toma, P. Breger, G. Mullot, F. Augé, Ph. Balcou, H. G. Muller, and P. Agostini, Observation of a train of attosecond pulses from high harmonic generation, Science **292**, 1689 (2001).

[13] H. G. Muller, Reconstruction of attosecond harmonic beating by interference of two-photon transitions, Appl. Phys. B **74**, s17 (2002).

[14] K. Amini, *et al.*, Symphony on strong field approximation, Rep. Prog. Phys. **82**, 116001 (2019).

[15] J. H. Eberly, Q. Su, and J. Javanainen, High-order harmonic production in multiphoton ionization, J. Opt. Soc. Am. B **6**, 1289 (1989).

[16] O. Smirnova and M. Ivanov, in *Attosecond and XUV Physics*, edited by T. Schultz and M. Vrakking, Chapter 7 (2013).

[17] J. Javanainen, J. H. Eberly, and Q. Su, Numerical simulations of multiphoton ionization and above-threshold electron spectra, Phys. Rev. A **38**, 3430 (1988).

[18] G. G. Paulus, W. Nicklich, H. Xu, P. Lambropoulos, and H. Walther, Plateau in above threshold ionization spectra, Phys. Rev. Lett. **72**, 2851 (1994).

[19] M. Lewenstein, K. C. Kulander, K. J. Schafer, and P. H. Bucksbaum, Rings in above-threshold ionization: A quasiclassical analysis, Phys. Rev. A **51**, 1495 (1995).

[20] S. P. Goreslavskii, S. V. Popruzhenko, R. Kopold, and W. Becker, Electron-electron correlation in laser-induced nonsequential double ionization, Phys. Rev. A **64**, 053402 (2001).

[21] S. V. Popruzhenko and D. Bauer, Strong field approximation for systems with Coulomb interaction, J. Mod. Opt. **55**, 2573 (2008).

[22] S. V. Popruzhenko, Keldysh theory of strong field ionization: History, applications, difficulties and perspectives, J. Phys. B: At. Mol. Opt. Phys. **47**, 204001 (2014).

[23] R. Blatt and C. F. Roos, Quantum simulations with trapped ions, Nat. Phys. **8**, 277 (2012).

[24] I. Bloch, J. Dalibard, and S. Nascimbène, Quantum simulations with ultracold quantum gases, Nat. Phys. **8**, 267 (2012).

[25] J. Ignacio Cirac and P. Zoller, Goals and opportunities in quantum simulation, Nat. Phys. **8**, 264 (2012).

[26] J. Argüello-Luengo, A. González-Tudela, T. Shi, P. Zoller, and J. Ignacio Cirac, Analogue quantum chemistry simulation, Nature **574**, 215 (2019).

[27] D.-S. Lühmann, C. Weitenberg, and K. Sengstock, Emulating molecular orbitals and electronic dynamics with ultracold atoms, Phys. Rev. X **5**, 031016 (2015).

[28] Y. Shen, Y. Lu, K. Zhang, J. Zhang, S. Zhang, J. Huh, and K. Kim, Quantum optical emulation of molecular vibronic spectroscopy using a trapped-ion device, Chem. Sci. **9**, 836 (2018).

[29] R. J. MacDonell, C. E. Dickerson, C. J. T. Birch, A. Kumar, C. L. Edmunds, M. J. Biercuk, C. Hempel, and I. Kassal, Analog quantum simulation of chemical dynamics, Chem. Sci. **12**, 9794 (2021).

[30] C. H. Valahu, V. C. Olaya-Agudelo, R. J. MacDonell, T. Navickas, A. D. Rao, M. J. Millican, J. B. Pérez-Sánchez, J. Yuen-Zhou, M. J. Biercuk, C. Hempel, T. R. Tan, and I. Kassal, Direct observation of geometric-phase interference in dynamics around a conical intersection, Nat. Chem. **15**, 1503 (2023).

[31] J. Whitlow, Z. Jia, Y. Wang, C. Fang, J. Kim, and K. R. Brown, Quantum simulation of conical intersections using trapped ions, Nat. Chem. **15**, 1509 (2023).

[32] A. Ben Levy, A. Hen, M. Kahn, Y. Aharon, T. Levin, N. Mazurski, U. Levy, and G. Marcus, Simulation of laser-induced tunnel ionization based on a curved waveguide, Sci. Rep. **13**, 12612 (2023).

[33] R. Senaratne, S. V. Rajagopal, T. Shimasaki, P. E. Dotti, K. M. Fujiwara, K. Singh, Z. A. Geiger, and D. M. Weld, Quantum simulation of ultrafast dynamics using trapped ultracold atoms, Nat. Commun. **9**, 2065 (2018).

[34] R. Dum, A. Sanpera, K.-A. Suominen, M. Brewczyk, M. Kuś, K. Rzazewski, and M. Lewenstein, Wave packet dynamics with Bose-Einstein condensates, Phys. Rev. Lett. **80**, 3899 (1998).

[35] S. Arlinghaus and M. Holthaus, Driven optical lattices as strong-field simulators, Phys. Rev. A **81**, 063612 (2010).

[36] S. Sala, J. Förster, and A. Saenz, Ultracold-atom quantum simulator for attosecond science, Phys. Rev. A **95**, 11403 (2017).

[37] M. Drescher, M. Hentschel, R. Kienberger, G. Tempea, Ch. Spielmann, G. A. Reider, P. B. Corkum, and F. Krausz, X-ray pulses approaching the attosecond frontier, Science **291**, 1923 (2001).

[38] F. Silva, S. M. Teichmann, S. L. Cousin, M. Hemmer, and J. Biegert, Spatiotemporal isolation of attosecond soft x-ray pulses in the water window, Nat. Commun. **6**, 6611 (2015).

[39] J. L. Krause, K. J. Schafer, and K. C. Kulander, High-order harmonic generation from atoms and ions in the high intensity regime, Phys. Rev. Lett. **68**, 3535 (1992).

[40] T. Popmintchev, *et al.*, Bright coherent ultrahigh harmonics in the keV x-ray regime from mid-infrared femtosecond lasers, Science **336**, 1287 (2012).

[41] Y. Kobayashi, T. Sekikawa, Y. Nabekawa, and S. Watanabe, 27-fs extreme ultraviolet pulse generation by high-order harmonics, Opt. Lett. **23**, 64 (1998).

[42] K. Midorikawa, Y. Nabekawa, and A. Suda, XUV multiphoton processes with intense high-order harmonics, Prog. Quantum Electron. **32**, 43 (2008).

[43] S. Chatziathanasiou, S. Kahaly, E. Skantzakis, G. Sansone, R. Lopez-Martens, S. Haessler, K. Varju, G. D. Tsakiris, D. Charalambidis, and P. Tzallas, Generation of attosecond light pulses from gas and solid state media, Photonics **4**, 26 (2017).

[44] N. Tsatrafyllis, B. Bergues, H. Schröder, L. Veisz, E. Skantzakis, D. Gray, B. Bodi, S. Kuhn, G. D. Tsakiris, D. Charalambidis, and P. Tzallas, The ion microscope as a tool for quantitative measurements in the extreme ultraviolet, Sci. Rep. **6**, 21556 (2016).

[45] B. Bergues, D. E. Rivas, M. Weidman, A. A. Muschet, W. Helml, A. Guggenmos, V. Pervak, U. Kleineberg, G. Marcus, R. Kienberger, D. Charalambidis, P. Tzallas, H. Schröder, F. Krausz, and L. Veisz, Tabletop nonlinear optics in the 100-eV spectral region, Optica **5**, 237 (2018).

[46] A. Nayak, I. Orfanos, I. Makos, M. Dumergue, S. Kühn, E. Skantzakis, B. Bodi, K. Varju, C. Kalpouzos, H. I. B. Banks, A. Emmanouilidou, D. Charalambidis, and P. Tzallas, Multiple ionization of argon via multi-XUV-photon absorption induced by 20-GW high-order harmonic laser pulses, Phys. Rev. A **98**, 023426 (2018).

[47] B. Senfftleben, M. Kretschmar, A. Hoffmann, M. Sauppe, J. Tümmler, I. Will, T. Nagy, M. J. J. Vrakking, D. Rupp, and B. Schütte, Highly non-linear ionization of atoms induced by intense high-harmonic pulses, J. Phys.: Photonics **2**, 034001 (2020).

[48] I. Orfanos, I. Makos, I. Liontos, E. Skantzakis, B. Major, A. Nayak, M. Dumergue, S. Kühn, S. Kahaly, K. Varju, G. Sansone, B. Witzel, C. Kalpouzos, L. A. A. Nikolopoulos, P. Tzallas, and D. Charalambidis, Non-linear processes in the extreme ultraviolet, J. Phys.: Photonics **2**, 042003 (2020).

[49] C. Gohle, T. Udem, M. Herrmann, J. Rauschenberger, R. Holzwarth, H. A. Schuessler, F. Krausz, and T. W. Hänsch, A frequency comb in the extreme ultraviolet, Nature **436**, 234 (2005).

[50] A. Cingöz, D. C. Yost, T. K. Allison, A. Ruehl, M. E. Fermann, I. Hartl, and J. Ye, Direct frequency comb spectroscopy in the extreme ultraviolet, Nature **482**, 68 (2012).

[51] R. E. F. Silva, I. V. Blinov, A. N. Rubtsov, O. Smirnova, and M. Ivanov, High-harmonic spectroscopy of ultrafast many-body dynamics in strongly correlated systems, Nat. Photonics **12**, 266 (2018).

[52] J. Alcalà, U. Bhattacharya, J. Biegert, M. Ciappina, U. Elu, T. Graß, P. T. Grochowski, M. Lewenstein, A. Palau, T. P. H. Sidiropoulos, T. Steinle, and I. Tyulnev, High-harmonic spectroscopy of quantum phase transitions in a high-T_c superconductor, Proc. Natl. Acad. Sci. **119**, e2207766119 (2022).

[53] A. L'Huillier, M. Lewenstein, P. Salières, Ph. Balcou, M. Yu. Ivanov, J. Larsson, and C. G. Wahlström, High-order harmonic-generation cutoff, Phys. Rev. A **48**, R3433 (1993).

[54] C. Lyngå, A. L'Huillier, and C.-G. Wahlström, High-order harmonic generation in molecular gases, J. Phys. B: At., Mol. Opt. Phys. **29**, 3293 (1996).

[55] S. Ghimire, A. D. DiChiara, E. Sistrunk, P. Agostini, L. F. DiMauro, and D. A. Reis, Observation of high-order harmonic generation in a bulk crystal, Nat. Phys. **7**, 138 (2011).

[56] E. Goulielmakis and T. Brabec, High harmonic generation in condensed matter, Nat. Photonics **16**, 411 (2022).

[57] L. Keldysh, Ionization of atoms in an alternating electric field, Sov. Phys. JETP **20**, 1307 (1965).

[58] P. Mulser and D. Bauer, in *High Power Laser-Matter Interaction*, edited by Peter Mulser and Dieter Bauer, Springer Tracts in Modern Physics (Springer, Berlin, Heidelberg, 2010), p. 267.

[59] P. B. Corkum, Plasma perspective on strong field multiphoton ionization, Phys. Rev. Lett. **71**, 1994 (1993).

[60] K. C. Kulander, K. J. Schafer, and J. L. Krause, in *Super-Intense Laser-Atom Physics*, edited by Bernard Piraux, Anne L'Huillier, and Kazimierz Rzaąewski, NATO ASI Series (Springer US, Boston, Massachusetts, 1993), p. 95.

[61] K. S. Budil, P. Salières, A. L'Huillier, T. Ditmire, and M. D. Perry, Influence of ellipticity on harmonic generation, Phys. Rev. A **48**, R3437 (1993).

[62] N. H. Burnett, C. Kan, and P. B. Corkum, Ellipticity and polarization effects in harmonic generation in ionizing neon, Phys. Rev. A **51**, R3418 (1995).

[63] F. A. Weihe, S. K. Dutta, G. Korn, D. Du, P. H. Bucksbaum, and P. L. Shkolnikov, Polarization of high-intensity high-harmonic generation, Phys. Rev. A **51**, R3433 (1995).

[64] F. A. Weihe and P. H. Bucksbaum, Measurement of the polarization state of high harmonics generated in gases, JOSA B **13**, 157 (1996).

[65] P. Antoine, B. Carré, A. L'Huillier, and M. Lewenstein, Polarization of high-order harmonics, Phys. Rev. A **55**, 1314 (1997).

[66] D. Schulze, M. Dörr, G. Sommerer, J. Ludwig, P. V. Nickles, T. Schlegel, W. Sandner, M. Drescher, U. Kleineberg, and U. Heinzmann, Polarization of the 61st harmonic from 1053-nm laser radiation in neon, Phys. Rev. A **57**, 3003 (1998).

[67] W. Becker, A. Lohr, and M. Kleber, Effects of rescattering on above-threshold ionization, J. Phys. B: At., Mol. Opt. Phys. **27**, L325 (1994).

[68] P. Antoine, A. L'Huillier, M. Lewenstein, P. Salières, and B. Carré, Theory of high-order harmonic generation by an elliptically polarized laser field, Phys. Rev. A **53**, 1725 (1996).

[69] A. Fleischer, O. Kfir, T. Diskin, P. Sidorenko, and O. Cohen, Spin angular momentum and tunable polarization in high-harmonic generation, Nat. Photonics **8**, 543 (2014).

[70] O. Kfir, P. Grychtol, E. Turgut, R. Knut, D. Zusin, D. Popmintchev, T. Popmintchev, H. Nembach, J. M. Shaw, A. Fleischer, H. Kapteyn, M. Murnane, and O. Cohen, Generation of bright phase-matched circularly-polarized extreme ultraviolet high harmonics, Nat. Photonics **9**, 99 (2015).

[71] D. B. Milošević, W. Becker, and R. Kopold, Generation of circularly polarized high-order harmonics by two-color coplanar field mixing, Phys. Rev. A **61**, 063403 (2000).

[72] E. Pisanty, S. Sukiasyan, and M. Ivanov, Spin conservation in high-order-harmonic generation using bicircular fields, Phys. Rev. A **90**, 043829 (2014).

[73] E. Pisanty Alatorre, Ph.D. thesis, 2016.

[74] P. Agostini, F. Fabre, G. Mainfray, G. Petite, and N. K. Rahman, Free-free transitions following six-photon ionization of xenon atoms, Phys. Rev. Lett. **42**, 1127 (1979).

[75] N. B. Delone and V. P. Kraĭnov, *Multiphoton Processes in Atoms* (Springer Science & Business Media, Heidelberg, 2000), 2nd ed.

[76] D. B. Milošević, G. G. Paulus, D. Bauer, and W. Becker, Above-threshold ionization by few-cycle pulses, J. Phys. B: At. Mol. Opt. Phys. **39**, R203 (2006).

[77] P. Agostini and L. F. DiMauro, in *Advances In Atomic, Molecular, and Optical Physics*, Vol. 61, edited by Paul Berman, Ennio Arimondo, and Chun Lin (Academic Press, San Diego, 2012), p. 117.

[78] A. l'Huillier, L. A. Lompre, G. Mainfray, and C. Manus, Multiply charged ions induced by multiphoton absorption in rare gases at 0.53 μm, Phys. Rev. A **27**, 2503 (1983).

[79] B. Walker, B. Sheehy, L. F. DiMauro, P. Agostini, K. J. Schafer, and K. C. Kulander, Precision measurement of strong field double ionization of helium, Phys. Rev. Lett. **73**, 1227 (1994).

[80] B. Feuerstein, R. Moshammer, D. Fischer, A. Dorn, C. D. Schröter, J. Deipenwisch, J. R. Crespo Lopez-Urrutia, C. Höhr, P. Neumayer, J. Ullrich, H. Rottke, C. Trump, M. Wittmann, G. Korn, and W. Sandner, Separation of recollision mechanisms in nonsequential strong field double ionization of Ar: The role of excitation tunneling, Phys. Rev. Lett. **87**, 043003 (2001).

[81] C. Figueira de Morisson Faria and X. Liu, Electron-electron correlation in strong laser fields, J. Mod. Opt. **58**, 1076 (2011).

[82] W. Becker, X. Liu, P. J. Ho, and J. H. Eberly, Theories of photoelectron correlation in laser-driven multiple atomic ionization, Rev. Mod. Phys. **84**, 1011 (2012).

[83] P. Hansch, M. A. Walker, and L. D. Van Woerkom, Resonant hot-electron production in above-threshold ionization, Phys. Rev. A **55**, R2535 (1997).

[84] M. Born and R. Oppenheimer, Zur Quantentheorie der Molekeln, Ann. Phys. **389**, 457 (1927).

[85] P. Atkins and R. Friedman, in *Molecular Quantum Mechanics* (Oxford University Press, Oxford, 2015), Chapter 8, p. 249.

[86] R. P. Feynman, Simulating physics with computers, Int. J. Theor. Phys. **21**, 7 (1982).

[87] S. Lloyd, Universal quantum simulators, Science **273**, 1073 (1996).

[88] J. M. Arrazola, *et al.*, Quantum circuits with many photons on a programmable nanophotonic chip, Nature **591**, 54 (2021).

[89] F. Arute, *et al.*, Quantum supremacy using a programmable superconducting processor, Nature **574**, 505 (2019).

[90] F. Arute, *et al.*, Google AI Quantum and collaborators, Hartree-Fock on a superconducting qubit quantum computer, Science **369**, 1084 (2020).

[91] J.-J. Choi, S. Hild, J. Zeiher, P. Schauß, A. Rubio-Abadal, T. Yefsah, V. Khemani, D. A. Huse, I. Bloch, and C. Gross, Exploring the many-body localization transition in two dimensions, Science **352**, 1547 (2016).

[92] S. Trotzky, Y.-A. Chen, A. Flesch, I. P. McCulloch, U. Schollwöck, J. Eisert, and I. Bloch, Probing the relaxation towards equilibrium in an isolated strongly correlated one-dimensional Bose gas, Nat. Phys. **8**, 325 (2012).

[93] A. J. Daley, I. Bloch, C. Kokail, S. Flannigan, N. Pearson, M. Troyer, and P. Zoller, Practical quantum advantage in quantum simulation, Nature **607**, 667 (2022).

[94] M. Greiner, O. Mandel, T. Esslinger, T. W. Hänsch, and I. Bloch, Quantum phase transition from a superfluid to a Mott insulator in a gas of ultracold atoms, Nature **415**, 39 (2002).

[95] R. Jördens, N. Strohmaier, K. Günter, H. Moritz, and T. Esslinger, A Mott insulator of fermionic atoms in an optical lattice, Nature **455**, 204 (2008).

[96] D. Jaksch, C. Bruder, J. I. Cirac, C. W. Gardiner, and P. Zoller, Cold bosonic atoms in optical lattices, Phys. Rev. Lett. **81**, 3108 (1998).

[97] C. Schweizer, F. Grusdt, M. Berngruber, L. Barbiero, E. Demler, N. Goldman, I. Bloch, and M. Aidelsburger, Floquet approach to $\mathbb{Z}_2$ lattice gauge theories with ultracold atoms in optical lattices, Nat. Phys. **15**, 1168 (2019).

[98] F. Görg, K. Sandholzer, J. Minguzzi, R. Desbuquois, M. Messer, and T. Esslinger, Realization of density-dependent Peierls phases to engineer quantized gauge fields coupled to ultracold matter, Nat. Phys. **15**, 1161 (2019).

[99] M. Aidelsburger, *et al.*, Cold atoms meet lattice gauge theory, Philos. Trans. R. Soc. A: Math. Phys. Eng. Sci. **380**, 20210064 (2022).

[100] A. Frölian, C. S. Chisholm, E. Neri, C. R. Cabrera, R. Ramos, A. Celi, and L. Tarruell, Realizing a 1D topological gauge theory in an optically dressed BEC, Nature **608**, 293 (2022).

[101] M. H. Anderson, J. R. Ensher, M. R. Matthews, C. E. Wieman, and E. A. Cornell, Observation of Bose-Einstein condensation in a dilute atomic vapor, Science **269**, 198 (1995).

[102] K. B. Davis, M. O. Mewes, M. R. Andrews, N. J. van Druten, D. S. Durfee, D. M. Kurn, and W. Ketterle, Bose-Einstein condensation in a gas of sodium atoms, Phys. Rev. Lett. **75**, 3969 (1995).

[103] B. D. Esry, Hartree-Fock theory for Bose-Einstein condensates and the inclusion of correlation effects, Phys. Rev. A **55**, 1147 (1997).

[104] S. V. Rajagopal, K. M. Fujiwara, R. Senaratne, K. Singh, Z. A. Geiger, and D. M. Weld, Quantum emulation of extreme non-equilibrium phenomena with trapped atoms, Ann. Phys. **529**, 1700008 (2017).
[105] V. Boyer, R. M. Godun, G. Smirne, D. Cassettari, C. M. Chandrashekar, A. B. Deb, Z. J. Laczik, and C. J. Foot, Dynamic manipulation of Bose-Einstein condensates with a spatial light modulator, Phys. Rev. A **73**, 031402 (2006).
[106] D. McGloin, G. C. Spalding, H. Melville, W. Sibbett, and K. Dholakia, Applications of spatial light modulators in atom optics, Opt. Express **11**, 158 (2003).
[107] C. Muldoon, L. Brandt, J. Dong, D. Stuart, E. Brainis, M. Himsworth, and A. Kuhn, Control and manipulation of cold atoms in optical tweezers, New J. Phys. **14**, 073051 (2012).
[108] Y.-X. Ren, R.-D. Lu, and L/ Gong, Tailoring light with a digital micromirror device, Ann. Phys. **527**, 447 (2015).
[109] T. Sato, K. L. Ishikawa, I. Březinová, F. Lackner, S. Nagele, and J. Burgdörfer, Time-dependent complete-active-space self-consistent-field method for atoms: Application to high-order harmonic generation, Phys. Rev. A **94**, 023405 (2016).
[110] R. Reiff, T. Joyce, A. Jaroń-Becker, and A. Becker, Single-active electron calculations of high-order harmonic generation from valence shells in atoms for quantitative comparison with TDDFT calculations, J. Phys. Commun. **4**, 065011 (2020).
[111] Q. Su and J. H. Eberly, Model atom for multiphoton physics, Phys. Rev. A **44**, 5997 (1991).
[112] L. A. Collins and A. L. Merts, Model calculations for an atom interacting with an intense, time-dependent electric field, Phys. Rev. A **37**, 2415 (1988).
[113] S. Geltman, Ionization of a model atom by a pulse of coherent radiation, J. Phys. B: At. Mol. Phys. **10**, 831 (1977).
[114] C. T. Fancher, A. J. Pyle, A. P. Rotunno, and S. Aubin, Microwave ac Zeeman force for ultracold atoms, Phys. Rev. A **97**, 043430 (2018).
[115] Y.-J. Lin, R. L. Compton, K. Jiménez-García, J. V. Porto, and I. B. Spielman, Synthetic magnetic fields for ultracold neutral atoms, Nature **462**, 628 (2009).
[116] R. Ma, M. Eric Tai, P. M. Preiss, W. S. Bakr, J. Simon, and M. Greiner, Photon-assisted tunneling in a biased strongly correlated Bose gas, Phys. Rev. Lett. **107**, 095301 (2011).
[117] M. R. Miller, Ph.D. thesis, University of Colorado Boulder, 2016. https://scholar.colorado.edu/concern/graduate_thesis_or_dissertations/bk128992v.
[118] A. Gordon and F. X. Kärtner, Quantitative modeling of single atom high harmonic generation, Phys. Rev. Lett. **95**, 223901 (2005).
[119] J. C. Baggesen and L. B. Madsen, On the dipole, velocity and acceleration forms in high-order harmonic generation from a single atom or molecule, J. Phys. B: At. Mol. Opt. Phys. **44**, 115601 (2011).
[120] V.-M. Gkortsas, S. Bhardwaj, E. L. Falcão-Filho, K.-H. Hong, A. Gordon, and F. X. Kärtner, Scaling of high harmonic generation conversion efficiency, J. Phys. B: At. Mol. Opt. Phys. **44**, 045601 (2011).
[121] H. R. Reiss, Limits on tunneling theories of strong-field ionization, Phys. Rev. Lett. **101**, 043002 (2008).
[122] M. B. Gaarde, J. L. Tate, and K. J. Schafer, Macroscopic aspects of attosecond pulse generation, J. Phys. B: At. Mol. Opt. Phys. **41**, 132001 (2008).
[123] S. E. Pollack, D. Dries, M. Junker, Y. P. Chen, T. A. Corcovilos, and R. G. Hulet, Extreme tunability of interactions in a ^{7}Li Bose-Einstein condensate, Phys. Rev. Lett. **102**, 090402 (2009).
[124] A. Bergschneider, V. M. Klinkhamer, J. H. Becher, R. Klemt, G. Zürn, P. M. Preiss, and S. Jochim, Spin-resolved single-atom imaging of ^{6}Li in free space, Phys. Rev. A **97**, 063613 (2018).
[125] M. Lewenstein, A. Sanpera, and V. Ahufinger, *Ultracold Atoms in Optical Lattices: Simulating Quantum Many-Body Systems* (Oxford University Press, Oxford, 2012).
[126] C. Chin, R. Grimm, P. Julienne, and E. Tiesinga, Feshbach resonances in ultracold gases, Rev. Mod. Phys. **82**, 1225 (2010).
[127] F. Nogrette, H. Labuhn, S. Ravets, D. Barredo, L. Béguin, A. Vernier, T. Lahaye, and A. Browaeys, Single-atom trapping in holographic 2D arrays of microtraps with arbitrary geometries, Phys. Rev. X **4**, 021034 (2014).
[128] D. Bluvstein, H. Levine, G. Semeghini, T. T. Wang, S. Ebadi, M. Kalinowski, A. Keesling, N. Maskara, H. Pichler, M. Greiner, V. Vuletić, and M. D. Lukin, A quantum processor based on coherent transport of entangled atom arrays, Nature **604**, 451 (2022).
[129] A. Gorlach, M. Even Tzur, M. Birk, M. Krüger, N. Rivera, O. Cohen, and I. Kaminer, High-harmonic generation driven by quantum light, Nat. Phys. **19**, 1689 (2023).
[130] P. Stammer, On the limitations of the semi-classical picture in high harmonic generation, preprint ArXiv:2308.15087 (accepted Nat. Phys.).
[131] P. Stammer, On the role of the optical phase and coherence in high harmonic generation, preprint ArXiv:2309.05010.
[132] M. E. Tzur, M. Birk, A. Gorlach, M. Krüger, I. Kaminer, and O. Cohen, Photon-statistics force in ultrafast electron dynamics, Nat. Photonics **17**, 501 (2023).
[133] S. Baier, M. J. Mark, D. Petter, K. Aikawa, L. Chomaz, Z. Cai, M. Baranov, P. Zoller, and F. Ferlaino, Extended Bose-Hubbard models with ultracold magnetic atoms, Science **352**, 201 (2016).
[134] E. Guardado-Sanchez, B. M. Spar, P. Schauss, R. Belyansky, J. T. Young, P. Bienias, A. V. Gorshkov, T. Iadecola, and W. S. Bakr, Quench dynamics of a Fermi gas with strong nonlocal interactions, Phys. Rev. X **11**, 021036 (2021).
[135] N. Šibalić and C. S. Adams, *Rydberg physics* (IOP Publishing, Bristol, 2018). https://iopscience.iop.org/book/mono/978-0-7503-1635-4.
[136] J. Argüello-Luengo, T. Shi, and A. González-Tudela, Engineering analog quantum chemistry Hamiltonians using cold atoms in optical lattices, Phys. Rev. A **103**, 043318 (2021).
[137] D. E. Chang, J. S. Douglas, A. González-Tudela, C. L. Hung, and H. J. Kimble, Colloquium: Quantum matter built from nanoscopic lattices of atoms and photons, Rev. Mod. Phys. **90**, 031002 (2018).
[138] Th. Weber, H. Giessen, M. Weckenbrock, G. Urbasch, A. Staudte, L. Spielberger, O. Jagutzki, V. Mergel,

M. Vollmer, and R. Dörner, Correlated electron emission in multiphoton double ionization, Nature **405**, 658 (2000).

[139] R. Moshammer, B. Feuerstein, W. Schmitt, A. Dorn, C. D. Schröter, J. Ullrich, H. Rottke, C. Trump, M. Wittmann, G. Korn, K. Hoffmann, and W. Sandner, Momentum distributions of Ne^{n+} ions created by an intense ultrashort laser pulse, Phys. Rev. Lett. **84**, 447 (2000).

[140] Th. Weber, M. Weckenbrock, A. Staudte, L. Spielberger, O. Jagutzki, V. Mergel, F. Afaneh, G. Urbasch, M. Vollmer, H. Giessen, and R. Dörner, Recoil-ion momentum distributions for single and double ionization of helium in strong laser fields, Phys. Rev. Lett. **84**, 443 (2000).

[141] A. Rudenko, V. L. B. De Jesus, Th. Ergler, K. Zrost, B. Feuerstein, C. D. Schröter, R. Moshammer, and J. Ullrich, Correlated two-electron momentum spectra for strong-field nonsequential double ionization of He at 800 nm, Phys. Rev. Lett. **99**, 263003 (2007).

[142] A. Staudte, C. Ruiz, M. Schöffler, S. Schössler, D. Zeidler, Th. Weber, M. Meckel, D. M. Villeneuve, P. B. Corkum, A. Becker, and R. Dörner, Binary and recoil collisions in strong field double ionization of helium, Phys. Rev. Lett. **99**, 263002 (2007).

[143] E. N. Osika, A. Chacón, L. Ortmann, N. Suárez, J. A. Pérez-Hernández, B. Szafran, M. F. Ciappina, F. Sols, A. S. Landsman, and M. Lewenstein, Wannier-Bloch approach to localization in high-harmonics generation in solids, Phys. Rev. X **7**, 021017 (2017).

[144] A. M. Parks, G. Ernotte, A. Thorpe, C. R. McDonald, P. B. Corkum, M. Taucer, and T. Brabec, Wannier quasi-classical approach to high harmonic generation in semiconductors, Optica **7**, 1764 (2020).

[145] G. Vampa, C. R. McDonald, G. Orlando, D. D. Klug, P. B. Corkum, and T. Brabec, Theoretical analysis of high-harmonic generation in solids, Phys. Rev. Lett. **113**, 073901 (2014).

[146] P. C. Becker, H. L. Fragnito, C. H. Brito Cruz, R. L. Fork, J. E. Cunningham, J. E. Henry, and C. V. Shank, Femtosecond photon echoes from band-to-band transitions in GaAs, Phys. Rev. Lett. **61**, 1647 (1988).

[147] M. T. Portella, J.-Y. Bigot, R. W. Schoenlein, J. E. Cunningham, and C. V. Shank, *k*-space carrier dynamics in GaAs, Appl. Phys. Lett. **60**, 2123 (1992).

[148] M. Kolesik and J. V. Moloney, Numerical discreteness and dephasing in high-harmonic calculations in solids, Phys. Rev. B **108**, 115433 (2023).

[149] I. Kilen, M. Kolesik, J. Hader, J. V. Moloney, U. Huttner, M. K. Hagen, and S. W. Koch, Propagation induced dephasing in semiconductor high-harmonic generation, Phys. Rev. Lett. **125**, 083901 (2020).

[150] G. G. Brown, Á. Jiménez-Galán, R. E. F. Silva, and M. Ivanov, A real-space perspective on dephasing in solid-state high harmonic generation, ArXiv:2210.16889 (2022).

[151] L. Yue and M. B. Gaarde, Imperfect recollisions in high-harmonic generation in solids, Phys. Rev. Lett. **124**, 153204 (2020).

[152] K. Drese and M. Holthaus, Ultracold atoms in modulated standing light waves, Chem. Phys. Dyn. Driven Quantum Syst. **217**, 201 (1997).

[153] J. L. Krause, K. J. Schafer, and K. C. Kulander, Calculation of photoemission from atoms subject to intense laser fields, Phys. Rev. A **45**, 4998 (1992).

[154] M. D. Feit, J. A. Fleck, and A. Steiger, Solution of the Schrödinger equation by a spectral method, J. Comput. Phys. **47**, 412 (1982).